A Study of the Magnetic Structure of $LaMn_2O_5$ from Neutron Powder Diffraction Data

Angel Muñoz,*[a] Jose A. Alonso,[b] María T. Casais,[b] María J. Martínez-Lope,[b] Jose L. Martínez,[b] and María T. Fernández-Díaz[c]

Keywords: Lanthanides / Magnetic properties / Neutron diffraction / Spin glass / Superexchange interaction

Polycrystalline $LaMn_2O_5$ has been studied by neutron powder diffraction in conjunction with magnetization data. The crystal structure of this oxide contains infinite chains of edge-sharing $Mn^{4+}O_6$ octahedra, interconnected by $Mn^{3+}O_5$ pyramids and LaO_8 units. Susceptibility measurements show that $LaMn_2O_5$ presents an antiferromagnetic order below a T_N value of about 31 K. Neutron diffraction experiments confirm the long-range ordering below this temperature in a magnetic structure characterized by the propagation vector $\mathbf{k}$ = (0,0,1/2). The magnetic arrangement is defined by the basis vectors $(G_x,A_y,0)$ and $(0,0,C'_z)$ for the Mn^{4+} and Mn^{3+} ions, respectively. At 3.5 K, the magnetic moments are 2.59(4) and 1.61(7) μ_B for the Mn^{3+} (4h site) and Mn^{4+} ions (4f site), respectively. Superexchange interactions between the Mn^{4+} ions through Mn^{4+}–O–Mn^{4+} paths are considered in order to explain the commensurate character of the magnetic structure in comparison with the incommensurate structures observed for most of the RMn_2O_5 (R = rare earth metal) compounds. A spin-glass-type behaviour, which probably involves the short-range order in the Mn^{3+} sublattice, is observed above T_N.

Introduction

The discovery of a colossal magnetoresistance effect in the hole-doped rare-earth manganites $R_{1-x}A_xMnO_3$ (A = alkaline-earth metal)[1,2] has triggered the investigation of related oxides which could also present similar phenomena, in particular complex oxides containing manganese ions in a mixed-valence state. The RMn_2O_5 (R = rare-earth metal, Y or Bi) family of oxides is appealing since it contains two different oxidation states for Mn, which are located at crystallographically distinct oxygen environments. According to the first crystallographic studies devoted to the RMn_2O_5 series in the 1960s, they present an orthorhombic crystallographic structure (*Pbam*),[3,4] which was confirmed by a recent high-resolution neutron powder diffraction study[5,6] for most of the compounds of the family. The two different sites for Mn − 4f and 4h − correspond to the Mn^{4+} and Mn^{3+} oxidation states, respectively. The Mn^{4+} ions are octahedrally coordinated by oxygen atoms, and the Mn^{3+} ions are bonded to five oxygen atoms in a distorted tetragonal pyramid. Along the *c* axis the crystallographic structure contains infinite chains of edge-sharing $Mn^{4+}O_6$ octahedra. The different chains are interconnected by dimer units of the $Mn^{3+}O_5$ pyramids. The R^{3+} cations form RO_8 units, which can be considered as bicapped trigonal prisms.

As regards the magnetic properties of the RMn_2O_5 oxides, initial reports[7,8] indicated an antiferromagnetic (AFM) behaviour below 40 K. In particular, for R = Nd, Tb, Ho, Er and Y the magnetic structure is characterized by the propagation vector $\mathbf{k} = (1/2,0,\tau)$ and the Mn spins are ordered according to a helicoidal structure, with the magnetic moments lying in the *ab* plane. In some of these compounds a magnetic ordering is also observed for the rare-earth moments, but at a significantly lower temperature. It seems that the R^{3+} magnetic moments present a sinusoidal magnetic structure. A further study for the compounds with R = Er and Tb[9] indicated that the magnetic structure for the Mn ions is also sinusoidally modulated. Some compounds of the family, such as $DyMn_2O_5$, present a more complicated ordering;[10] its magnetic structure is defined by two propagation vectors, $\mathbf{k_1} = (1/2,0,0)$ and $\mathbf{k_2} = (1/2,0,\tau)$. The magnetic structure of $EuMn_2O_5$ has also been analysed to a certain degree. Its magnetic structure is characterised by $\mathbf{k} = (1/2,0,\tau)$; τ varies with the temperature and remains constant for $T < 6$ K on achieving the commensurable value $\tau = 1/3$.[11] Unlike most of the RMn_2O_5 compounds, $BiMn_2O_5$ presents a commensurate magnetic structure,[12,13] defined by $\mathbf{k} = (1/2,0,1/2)$.

Dielectric and magnetoelectric studies[14,15] carried out on the RMn_2O_5 oxides indicate the presence of ferroelecticity in these compounds. Many studies have been performed

---

[a] Dpto. Física Aplicada, EPS, Universidad Carlos III
Avda. Universidad 30, 28911 Leganés-Madrid, Spain
Fax: +34-91-624-8749
E-mail: amunoz@fis.uc3m.es
[b] Instituto de Ciencia de Materiales de Madrid, CSIC
Cantoblanco, 28049 Madrid, Spain
[c] Institut Laue Langevin
B. P. 156X, 38042 Grenoble, France

DOI: 10.1002/ejic.200400548

in order to characterize the coexistence of ferroelectricity and magnetism, in particular the effect on the ferroelectric properties when a magnetic field is applied. Very recently,[16] in the multiferroic $TbMn_2O_5$ compound, a strong interplay between electrical polarization and the applied magnetic field has been reported, even for small fields. This striking behaviour implies a new possible device application consisting of magnetically recorded ferroelectric memory.

The preparation and crystal structure of $LaMn_2O_5$ has not been described until recently,[6] since its synthesis requires the use of high oxygen pressure. The aim of this paper is to report on the magnetic ordering and its thermal evolution from neutron diffraction measurements for this material, in conjunction with magnetic susceptibility measurements. A comparison with the magnetic structure of other compounds of the series is also established.

Results

Magnetic Measurements

The dc magnetic susceptibility curves recorded under zero-field-cooling (ZFC) and under field-cooling (FC) conditions are shown in Figure 1. Both curves present a similar behaviour above a T_N value of about 31 K; they diverge below this temperature [see inset (a) of Figure 1]. As will be shown for the neutron diffraction results, this temperature coincides with the establishment of the long-range magnetic ordering in $LaMn_2O_5$. The evolution of the FC susceptibility below T_N corresponds to the onset of an AFM ordering. Another important feature of the dc susceptibility curve is the presence of a very broad maximum at low temperature, which is centred at around 45 K (T_{SG}). A broad maximum is also observed in the real part of the ac susceptibility (see Figure 2). As is shown in inset (a) of Figure 2, the thermal evolution of the ac curve strongly depends on the frequency, which suggests a spin-glass-like behaviour at low temperature. It is well known that irreversibility in the spin-glass behaviour leads to a non-zero out-of-phase component, χ'' (imaginary part of the ac susceptibility). This can clearly be seen in inset (b) of Figure 2, which shows χ''. This confirms the spin-glass behaviour, and the presence of two peaks indicates that the freezing of the spin-glass state takes place in a complicated way.

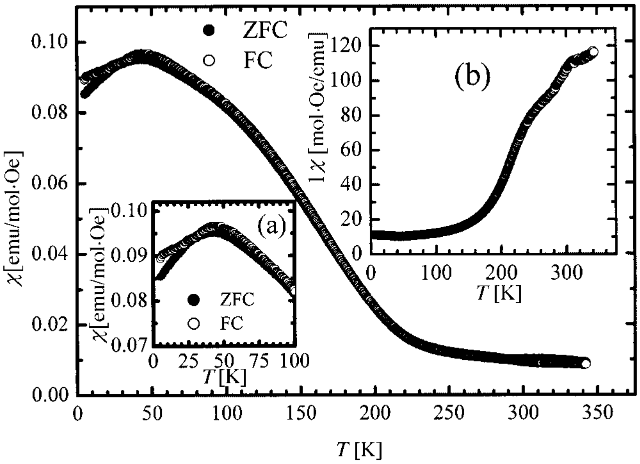

Figure 1. Thermal variation of the dc susceptibility under zero-field cooling (ZFC) and field-cooling (FC) conditions (H = 1 kOe); inset: (a) close-up of the low-temperature region; (b) plot of the reciprocal susceptibility (FC) versus temperature

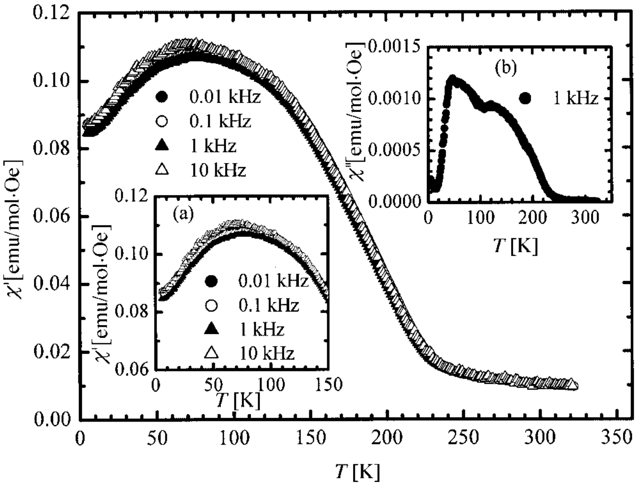

Figure 2. Real ac susceptibility curve; inset: (a) close-up of the low-temperature region; (b) imaginary component of the ac susceptibility

As regards the thermal variation of the dc susceptibility at high temperature, a linear behaviour in the reciprocal susceptibility is not observed below 300 K [inset (b) of Figure 1]. Applying the Curie–Weiss law in the temperature range 317–342 K gives a paramagnetic temperature, Θ_P, of –225 K and an effective magnetic moment of 6.25 μ_B. The effective magnetic moment is in good agreement with the theoretical value, determined as $\mu = [\mu^2(Mn^{3+}) + \mu^2(Mn^{4+})]^{1/2}$, of 6.24 μ_B, where the spin-only values of 4.90 and 3.87 μ_B are considered for the Mn^{3+} and Mn^{4+} ions, respectively. The magnetization curves displayed in Figure 3 show a negligible magnetization at low temperatures, discarding the presence of a weak ferromagnetism effect. We suggest that the change in the slope observed in the inverse of the susceptibility at around 275 K is due to crystal-field effects.

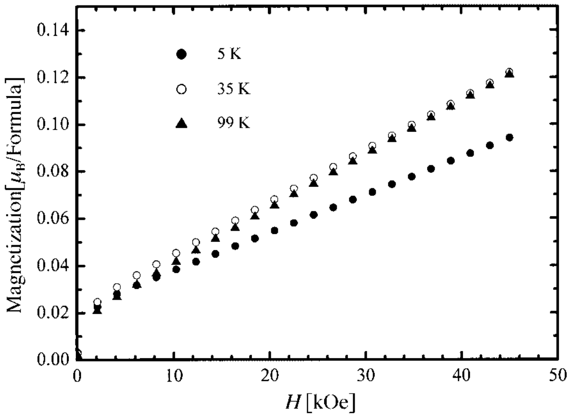

Figure 3. Isothermal magnetization curves at 5, 35 and 99 K

Magnetic Structure from Neutron Diffraction Measurements

A set of neutron powder diffraction (NPD) patterns acquired in the temperature range 3.5–98.8 K, with λ = 2.40 Å, has been used to determine the magnetic structure and study its thermal evolution. For the high-temperature NPD patterns, all the Bragg reflections can be indexed in the orthorhombic *Pbam* space group. The lattice parameters at 98.8 K refined to a = 7.6121(8) Å, b = 8.6372(8) Å and c = 5.6691(6) Å. On decreasing the temperature to below 31 K new peaks appeared in the patterns, thus confirming the onset of a magnetic ordering with a T_N value of 31 K (see Figure 4). The new peaks can be indexed with the propagation vector $\mathbf{k}$ = (0,0,1/2), which implies a commensurable magnetic structure with a magnetic unit-cell that doubles the chemical one along the c direction. As can be seen in Figure 5, the intensity of the magnetic reflections increases monotonically below T_N and reaches saturation at low temperature, with no anomalies that could indicate a modification of the long-range spin arrangement. Therefore, the magnetic structure seems to remain stable down to 3.5 K.

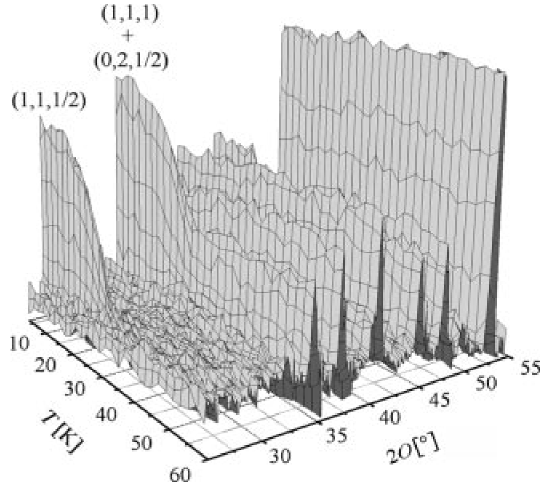

Figure 4. Thermal evolution of the NPD patterns for 3.5 < T < 60 K and 25° < 2θ < 55°

For the resolution of the magnetic structure, the solutions compatible with the symmetry of $LaMn_2O_5$ have been taken into consideration. The possible solutions were determined by a representation analysis of group theory technique described by Bertaut.[17] For $\mathbf{k}$ = (0,0,1/2), the irreducible representations of the $G_\mathbf{k}$ group are those given in Table 1, which have been taken from Kovalev's tables.[18] The basis vectors associated with each irreducible representation are reported in Table 2. The basis vectors define the different possible magnetic structures and were obtained by the projection operator technique. The notation for the Mn1 atoms located at the 4h site is 1(x,y,1/2), 2(–x,–y,1/2), 3(–x + 1/2,y + 1/2,1/2) and 4(x + 1/2,–y + 1/2,1/2). The Mn2 atoms of the 4f site are labelled as 5(1/2,0,z), 6(1/2,0,–z), 7(0,1/2,z) and 8(0,1/2,–z).

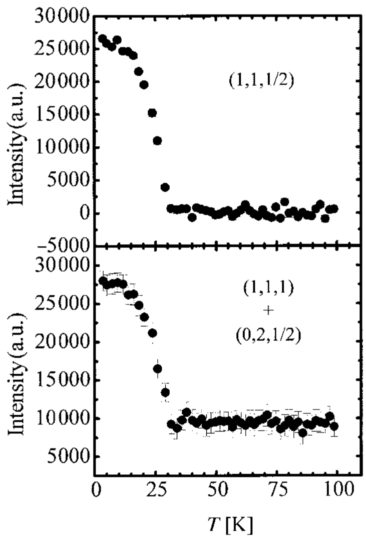

Figure 5. Thermal evolution of the magnetic reflections (1,1,1/2) and (0,2,1/2)

Table 1. Irreducible representations of the small group $G_\mathbf{k}$ for $\mathbf{k}$ = (0,0,1/2) following Kovalev's notation

	h_1	h_2/(**t**)	h_3/(**t**)	h_4	h_{25}	h_{26}/(**t**)	h_{27}/(**t**)	h_{28}
Γ_1	1	1	1	1	1	1	1	1
Γ_2	1	1	1	1	–1	–1	–1	–1
Γ_3	1	1	–1	–1	1	1	–1	–1
Γ_4	1	1	–1	–1	–1	–1	1	1
Γ_5	1	–1	1	–1	1	–1	1	–1
Γ_6	1	–1	1	–1	–1	1	–1	1
Γ_7	1	–1	–1	1	1	–1	–1	1
Γ_8	1	–1	–1	1	–1	1	1	–1

Table 2. Basis vectors for $LaMn_2O_5$

	Mn1 (4h)[a]	Mn2 (4f)[b]
Γ_1	(G_x,A_y,0)	(0,0,C'_z)
Γ_2	(0,0,F_z)	(0,0,G'_z)
Γ_3	(0,0,A_z)	(F'_x,C'_y,0)
Γ_4	(C_x,F_y,0)	(A'_x,G'_y,0)
Γ_5	(0,0,G_z)	(C'_x,F'_y,0)
Γ_6	(F_x,C_y,0)	(G'_x,A'_y,0)
Γ_7	(A_x,G_y,0)	(0,0,F'_z)
Γ_8	(0,0,C_z)	(0,0,A'_z)

[a] F = m1 + m2 + m3 + m4; C = m1 + m2 – m3 – m4; A = m1 – m2 – m3 + m4; G = m1 – m2 + m3 – m4. [b] F' = m5 + m6 + m7 + m8; C' = m5 + m6 – m7 – m8; A' = m5 – m6 – m7 + m8; G' = m5 – m6 + m7 – m8.

After checking the different solutions, the magnetic structure that shows the best agreement with the experimental data is defined by the basis vectors (G_x,A_y,0) for Mn1 atoms (site 4h) and (0,0,C'_z) for Mn2 atoms (site 4f). The calculated and observed NPD patterns for this solution at 3.5 K are compared in Figure 6. In the fitting, the atomic positions of $LaMn_2O_5$ are fixed to those given in Table 4 in the Exp. Sect. At 3.5 K, the magnetic moments are 2.59(4) and 1.61(7) μ_B for the Mn1 and Mn2 atoms, respectively (see Table 3). These values are significantly lower than those expected for the oxidation states Mn^{3+} at 4h sites (electronic configuration $t_{2g}^3e_g^1$, expected moment of 4 μ_B) and Mn^{4+} at 4f sites (electronic configuration t_{2g}^3, with 3 μ_B). This reduction could be due to covalency effects.

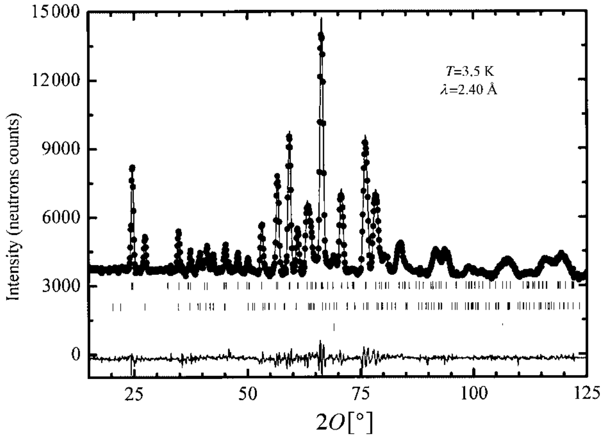

Figure 6. Observed (solid circles) and calculated (solid line) NPD patterns at 3.5 K; the first series of tick marks corresponds to the nuclear Bragg reflections of $LaMn_2O_5$, the second one to the magnetic reflections and the third one to the vanadium sample holder; the solid line at the bottom is the difference between the observed and calculated NPD patterns

The thermal evolution of the magnetic moments below T_N is displayed in Figure 7. On cooling, both the Mn1 and Mn2 ordered moments increase monotonically and reach saturation at low temperature. A view of the magnetic structure is presented in Figure 8. The magnetic moments of the Mn^{4+} ions are arranged along the *c* direction, whereas for the Mn^{3+} ions the moments are oriented in the *ab* plane. On the other hand, as displayed in Figure 8, the magnetic moments of the $z = z_0$ [$z_0 = 0.2610(8)$] and $z = -z_0$ layers, which are separated by a layer of La atoms, are ferromagnetically coupled. In contrast, the $z = z_0$ and $z = 1 - z_0$ layers, which are separated by a layer of Mn^{3+} ions, are antiferromagnetically coupled.

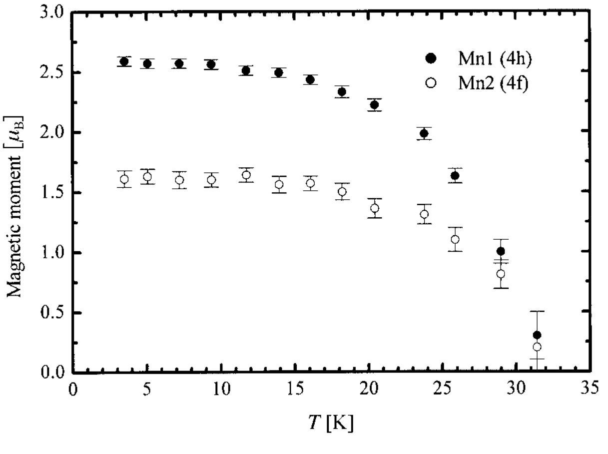

Figure 7. Thermal evolution of the magnetic moments for the Mn^{3+} (4h site) and Mn^{4+} (4f site) ions

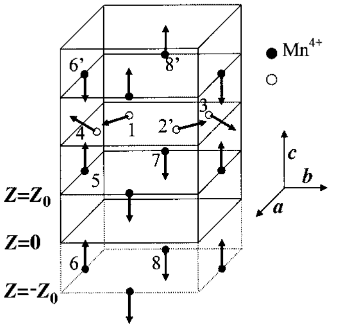

Figure 8. Schematic view of the magnetic structure; only the Mn atoms are represented; the primed atoms are related to the corresponding non-primed atoms by a lattice translation

Table 3. Results of the fitting of the NPD pattern at 3.5 K for the magnetic structure resolution

	Mn_1(4h)	Mn_2 (4f)
Solution	$(G_x,A_y,0)$	$(0,0,C'_z)$
Values (μ_B)	[2.28(4), –1.23(8),0]	[0,0,1.61(7)]
$\lvert m \rvert$ (μ_B)	2.59(4)	1.61(7)
Discrep. factors	R_B(Nuc.) = 2.4%; R_B(Magnet.) = 9.2%; χ^2 = 2.4	

The sequential refinement of the NPD patterns allowed us to determine the thermal evolution of the unit-cell parameters. The thermal variation of the *a* and *c* lattice parameters below 100 K is represented in Figure 9a. On decreasing the temperature below 100 K, the *c* lattice parameter decreases almost linearly and, below T_N, it remains virtually constant. Surprisingly, the *a* parameter increases with a sigmoidal shape when the temperature de-

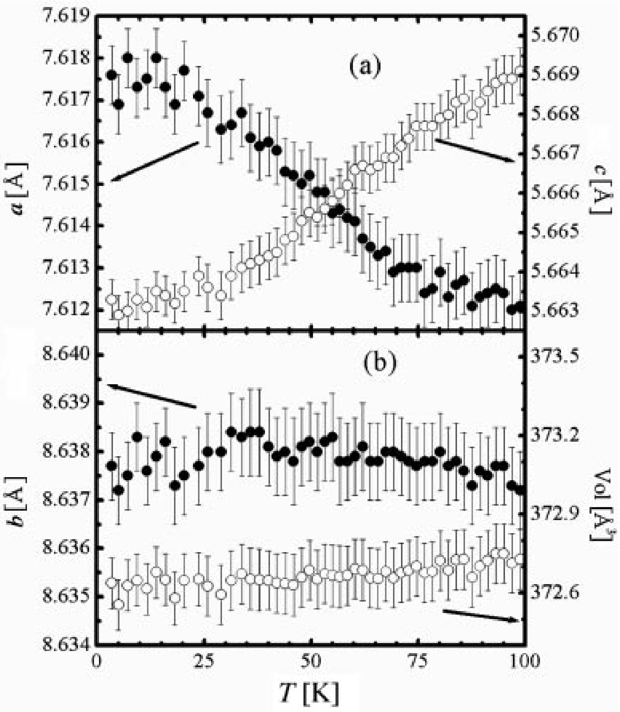

Figure 9. Thermal variation of the *a*, *b* and *c* lattice parameters and unit-cell volume

creases. The *b* lattice parameter variation (Figure 9b) also shows a slight anomaly around T_N, which suggests a subtle magnetostrictive effect. The unit-cell volume, averaging the trends of *a* and *c* parameters, remains constant over the whole temperature range.

Discussion

The neutron diffraction measurements have shown that $LaMn_2O_5$ orders below 31 K with a magnetic structure characterized by the propagation vector $\mathbf{k} = (0,0,1/2)$ and defined by the basis vectors $(G_x,A_y,0)$ and $(0,0,C'_z)$ for the Mn^{4+} and Mn^{3+} ions, respectively. For a better understanding of the spin arrangement it is very useful to bear in mind a description of the crystallographic structure. It consists of chains of edge-sharing $Mn^{4+}O_6$ octahedra arranged along the *c* axis. Along the chain direction, the $Mn^{4+}O_6$ octahedra (Mn2) are interleaved either by a layer of La^{3+} ions or by a layer of Mn^{3+} ions (Mn1). This implies that, for a given $Mn^{4+}O_6$ octahedron, there are two closer $Mn^{4+}O_6$ octahedra, one at $d_1 = 2z_0$ (separated by La^{3+} ions) and one at $d_2 = 1 - 2z_0$ (separated by Mn^{3+} ions). For $LaMn_2O_5$ the Mn2–Mn2 distances are d_1 = 2.987 Å and d_2 = 2.735 Å (Table 4). The different chains are interconnected by $La^{3+}O_8$ and $Mn^{3+}O_5$ units; these latter polyhedra mediate the magnetic coupling between neighbouring $Mn^{4+}O_6$ chains. In fact, the $Mn^{3+}O_5$ units form dimers of two pyramids related by an inversion centre. For $LaMn_2O_5$, the distance between the two Mn^{3+} ions within the dimer is 2.894 Å. The chains of $Mn^{4+}O_6$ octahedra, separated by a lattice parameter along *a* or *b*, are connected by a dimer. On the other hand, every chain has four closer chains interconnected by a single $Mn^{3+}O_5$ pyramid. This arrangement is displayed in Figure 10.

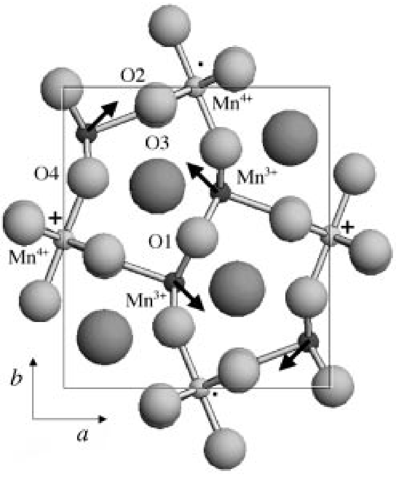

Figure 10. Projection of the crystallographic structure in the *ab* plane; the Mn^{3+} and Mn^{4+} ions are in the $z = 1/2$ and $z = 1 - z_0$ planes, respectively; the arrows indicate the direction of the Mn^{3+} magnetic moments in the *ab* plane; the + and – symbols indicate Mn^{4+} magnetic moments oriented parallel or antiparallel, respectively, to the direction of the *c* axis

In the magnetic structure, the magnetic moments of the Mn^{4+} ions are directed along *c* in the chains of $Mn^{4+}O_6$ octahedra (Figure 8). Within a single chain, the coupling between the Mn^{4+} ions of two adjacent octahedra separated by a La^{3+} layer is ferromagnetic, whereas those separated by a Mn^{3+} layer are antiferromagnetically coupled. Therefore, we have alternating FM and AFM couplings along the chains. To understand the observed magnetic arrangement, we must consider the following interactions: i) the superexchange interaction between the Mn^{4+} ions separated by an La^{3+} layer (with an Mn2–Mn2 distance, d_1, of 2.986 Å), across an Mn^{4+}–O2–Mn^{4+} path (with a bonding angle of 100.1°), assigned to the J_1 superexchange parameter; ii) the superexchange interaction between the Mn^{4+} ions separated by an Mn^{3+} layer, characterized by an Mn2–Mn2 distance, d_2, of 2.735 Å, across the superexchange path Mn^{4+}–O3–Mn^{4+} (bonding angle 93.3°), labelled J_2; and iii) the indirect superexchange interaction involving the $Mn^{3+}O_5$ units, across Mn^{4+}–O2–Mn^{3+}–O4–Mn^{4+} paths, characterized by J_3. If the indirect superexchange interaction is isotropic, J_3 would tend to couple the two Mn^{4+} ions placed at both sides of the Mn^{3+} layer ferromagnetically, as both these Mn^{4+} ions are symmetrically arranged with respect to the Mn^{3+} layer. The experimental results indicate that the coupling is AFM, which implies that J_2 must be negative and much greater than J_3. In the same way, J_1 must be positive, as the coupling between the Mn^{4+} ions separated by a La^{3+} layer is ferromagnetic. The presence of two superexchange interactions of different sign along *c* accounts for the propagation vector $\mathbf{k} = (0,0,1/2)$. Furthermore, it seems that a short Mn2–Mn2 distance along the chains favours an AFM interaction, whereas a long distance implies a ferromagnetic interaction. The J_1 and J_2 values depend on the distances d_1 and d_2, respectively. These distances are determined by the z_o position parameter for the Mn2 atoms (4f site). In the RMn_2O_5 series, on decreasing the R^{3+} ionic radius, d_1 tends to decrease; this changes makes possible the fulfilment of the condition $|J_1| < 4|J_2|$, which can give place to the incommensurate magnetic structure found in most of the RMn_2O_5 compounds ($k_z = \tau$).

On the other hand, every chain is antiferromagnetically coupled to four closer ones. In the dimers, the two Mn^{3+} ions are antiferromagnetically coupled and the magnetic moments are oriented in the *ab* plane in such a way that the moment direction is nearly perpendicular to the base of the pyramid. The path for the superexchange interaction between the Mn^{3+} ions of the dimer is Mn^{3+}–O1–Mn^{3+}, with a bonding angle of 97.5°. Taking into account the expected electronic configuration for Mn^{4+} and Mn^{3+} ions − t_{2g}^3 and $t_{2g}^3e_g^1$, respectively − the superexchange interaction across Mn^{4+}–O2–Mn^{4+} paths (along the chains) takes place via t_{2g}–t_{2g} orbitals, whereas for Mn^{3+}–O3–Mn^{3+} (within the dimers) it takes place via e_{2g}–e_{2g} orbitals. Given the directionality of the d orbitals, the latter superexchange interaction (via e_{2g}–e_{2g} orbitals) is, in general, stronger than that observed via t_{2g}–t_{2g} orbitals; this fact suggests that the coupling between Mn^{3+} moments within the dimers would take place at higher temperatures. We can consider a scenario consisting of the appearance of an AFM coupling in each dimer at temperatures well above T_N. This short-range ordering, with no coherence across the crystal, would be responsible for the spin-glass-type behaviour described above. On decreasing the temperature, the strengthening of the superexchange interactions between the Mn^{4+} ions (along the chains) and between Mn^{3+} and Mn^{4+} moments would give rise to the establishment of a long-range order below T_N.

It is worthwhile to compare the magnetic structure of $LaMn_2O_5$ with those of other members of the RMn_2O_5 family. For most RMn_2O_5 oxides the magnetic structure is defined by the propagation vector $\mathbf{k} = (1/2,0,\tau)$, except for $BiMn_2O_5$, where $\mathbf{k} = (1/2,0,1/2)$, and $DyMn_2O_5$, where $\mathbf{k_1} = (1/2,0,0)$ and $\mathbf{k_2} = (1/2,0,\tau)$. Thus, for all of them the magnetic structure propagates antiferromagnetically along the *a* direction, whereas for $LaMn_2O_5$, with $\mathbf{k} = (0,0,1/2)$, the propagation is ferromagnetic. As regards the orientation of the magnetic moments, in $LaMn_2O_5$ the moments of the Mn^{4+} ions are parallel to the *c* direction and for the rest of the compounds of the series the moments are in the *ab* plane. The magnetic anisotropy is mainly given by the symmetry of the ion environment, in this case by the symmetry of the $Mn^{4+}O_6$ octahedra. The Mn–O distances in the octahedra become more different as the R^{3+} ionic radius increases, so that the higher symmetry of the octahedra is found for $LaMn_2O_5$. The coupling of the magnetic moments of the Mn^{4+} ions along the *c* direction is also worth discussing. For RMn_2O_5 compounds with $\mathbf{k} = (1/2,0,\tau)$ two models[8] for the magnetic structure can be considered. In one of them, the coupling of the magnetic moments for the Mn^{4+} ions separated by an Mn^{3+} plane is ferromagnetic, and for those Mn^{4+} ions separated by an R^{3+} plane the magnetic moments form a certain angle, φ. In the second model, the coupling is simply the inverse. In fact, both $BiMn_2O_5$ and $LaMn_2O_5$ follow both models, but with $\varphi = 180°$ for $BiMn_2O_5$ (first model) the coupling of the magnetic moments for the Mn^{4+} ions separated by a R^{3+} plane is perfectly antiferromagnetic, whereas for $LaMn_2O_5$ the coupling is the opposite and follows the second model.

Conclusions

Both dc and ac magnetic susceptibility measurements show that $LaMn_2O_5$ undergoes an AFM ordering below 31 K (T_N), and also suggest a spin-glass-like behaviour above T_N. Neutron diffraction experiments allowed us to characterize the low-temperature magnetic arrangement: the magnetic structure is defined by the propagation vector $\mathbf{k} = (0,0,1/2)$, and the spin coupling is given by the basis vectors $(G_x,A_y,0)$ and $(0,0,C'_z)$ for the Mn^{4+} and Mn^{3+} spins, respectively. Within the chains of $Mn^{4+}O_6$ octahedra, the magnetic moments of the Mn^{4+} ions are directed along *c*; each Mn^{4+} moment displays an FM and an AFM coupling with neighbouring Mn^{4+} spins to account for the observed propagation vector. Adjacent chains are antiferromagnetically coupled. Within the dimer units of $Mn^{3+}O_5$ pyramids, the two Mn^{3+} spins also show an AFM coupling, with the magnetic moments lying in the *ab* plane. The magnitude of the two superexchange parameters defined along the chains, J_1 and J_2, is related to the two different distances between Mn2 atoms; the different sign and magnitude of J_1 and J_2 accounts for the commensurate character of the magnetic structure. We suggest that the two Mn^{3+} ions of each dimer unit are antiferromagnetically coupled above T_N, given the superior strength of the superexchange interactions through the e_{2g}–e_{2g} orbitals, which would cause a short-range magnetic order within the Mn^{3+} dimers, with no long-range coherence across the crystal. This effect would be responsible for the spin-glass-type behaviour observed in the magnetization measurements.

Experimental Section

$LaMn_2O_5$ was obtained as a dark-brown, polycrystalline powder starting from precursors previously synthesized by a wet-chemistry technique, followed by oxygenation at 1000 °C under 200 bar of oxygen pressure, as described elsewhere.[6] It is important to underline that the final treatment under high oxygen pressure is essential for the stabilization of monophase $LaMn_2O_5$. This material could not be obtained at ambient pressure starting either from citrate precursors or ceramic mixtures since the competitive, very stable $LaMnO_{3+\delta}$ perovskite was always present in the final product.

The magnetic measurements were performed in a PPMS (Quantum Design) system. The dc susceptibility curves were obtained under a 1 kOe magnetic field, under both zero-field cooling (ZFC) and field cooling (FC) conditions, for temperatures between 5.2 and 342.1 K. The ac susceptibility was measured in the temperature range 5–322 K under a small oscillating magnetic field of frequencies 0.01, 0.1, 1 and 10 kHz. Different isothermal magnetization curves were obtained at 5, 35 and 99 K in a magnetic field of between 0.05 and 45 kOe.

The study of the magnetic structure of $LaMn_2O_5$ was carried out from a set of neutron powder diffraction (NPD) patterns, collected at the high flux D20 diffractometer of the Institut Laue-Langevin in Grenoble (France). The patterns were dynamically acquired in the temperature range 3.5–98.8 K with a wavelength, λ, of 2.40 Å. The NPD data were analysed by the Rietveld method,[19] using the FULLPROF[20] program. The line-shape of the diffraction peaks was simulated by a Gaussian function and the background was fitted to a fifth-degree polynomial function. In the magnetic refinements, the atomic parameters were fixed to the values given in ref.[5], previously refined from high resolution NPD data, measured in the D2B diffractometer at the ILL-Grenoble on the same sample used in the present experiments. The atomic coordinates and main interatomic distances of $LaMn_2O_5$ taken from this reference are listed in Table 4.

Acknowledgments

We thank for financial support from the CICyT for the projects MAT2004-0479 and MAT2002-1329, and we are grateful to ILL for making all facilities available.

[1] R. M. Kusters, J. Singleton, D. A. Keen, R. McGreevy, W. Hayes, *Physica B* **1989**, *155*, 362.

[2] R. Von Helmolt, J. Wecker, B. Holzapfet, L. Schultz, K. Samwer, *Phys. Rev. Lett.* **1993**, *71*, 2331.

Table 4. Structural parameters for $LaMn_2O_5$ at room temperature and some selected interatomic distances[a]

	Atomic coordinates			Interatomic distances [Å]			
Atoms	*x*	*y*	*z*	$Mn^{3+}O_5$		$Mn^{4+}O_6$	
R (4g)	0.1451	0.1736	0.0000	Mn1–O1	(×2) 1.925	Mn2–O2	(×2) 1.948
Mn1(4h)	0.4114	0.3533	0.5000	Mn1–O3	2.120	Mn2–O3	(×2) 1.881
Mn2 (4f)	0.0000	0.5000	0.2610	Mn1–O4	(×2) 1.904	Mn2–O4	(×2) 1.932
O1 (4e)	0.0000	0.0000	0.2781	<Mn1–O>	1.956	<Mn2–O>	1.921
O2 (4)	0.1525	0.4497	0.0000	Mn1–Mn1	2.894		
O3 (4h)	0.1525	0.4374	0.5000	Mn2–Mn2	2.735		
O4 (8i)	0.4068	0.2061	0.2540	Mn2–Mn2	2.986		

[a] $a = 7.6823$ Å; $b = 8.7056$ Å; $c = 5.7214$ Å.

[3] S. Quezel-Ambrunaz, E. F. Bertaut, G. Buisson, *C. R. Acad. Sci.* **1964**, *258*, 3025.
[4] E. F. Bertaut, G. Buisson, A. Durif, A. Mareschal, M. C. Montmory, S. Quezel-Ambrunaz, *Bull. Soc. Chim. Fr.* **1965**, 1132.
[5] J. A. Alonso, M. T. Casais, M. J. Martínez-Lope, J. L. Martínez, M. T. Fernández-Díaz, *J. Phys.: Condens. Matter* **1997**, *9*, 8515–8526.
[6] J. A. Alonso, M. T. Casais, M. J. Martínez-Lope, I. Rasines, *J. Solid State Chem.* **1997**, *129*, 105–112.
[7] G. Buisson, *Phys. Status Solidi A* **1973**, *16*, 533.
[8] G. Buisson, *Phys. Status Solidi A* **1973**, *17*, 191.
[9] P. P. Gardner, C. Wilkinson, J. B. Forsyth, B. M. Wanklyn, *J. Phys. C: Solid State Phys.* **1988**, *21*, 5653.
[10] C. Wilkinson, F. Sinclair, P. P. Gardner, J. B. Forsyth, B. M. Wanklyn, *J. Phys. C: Solid State Phys.* **1981**, *14*, 1671.
[11] V. Polyakov, V. Plakhty, M. Bonnet, P. Burlet, L. P. Regnault, S. Gavrilov, I. Zobkalo, O. Smirnov, *Physica B* **2001**, *297*, 208.
[12] E. F. Bertaut, G. Buisson, S. Quezel-Ambrunaz, G. Quezel, *Solid State Commun.* **1967**, *5*, 25.
[13] A. Muñoz, J. A. Alonso, M. T. Casais, M. J. Martínez-Lope, J. L. Martínez, M. T. Fernández-Díaz, *Phys. Rev. B* **2002**, 65, 144 423.
[14] H. Tsujino, H. Komada, H. Tanaka, K. Kohn, in *Proceedings of the 6th International Conference on Ferrites* (Tokyo and Kyoto, 1992) (Eds.: M. Abe, T. Yamaguchi), Japan Society of Powder and Powder Metallurgy, Tokyo, **1992**, p. 714.
[15] K. Saito, K. Kohn, *J. Phys.: Condens. Matter* **1995**, *7*, 2855–2863.
[16] N. Hur, S. Park, P. A. Sharma, J. S. Ahn, S. Guha, S.-W. Cheong, *Nature* **2004**, *429*, 392.
[17] E. F. Bertaut, in *Magnetism* (Eds.: G. T. Rado, H. Shul), Academic Press, New York, **1963**, vol. III, chapter 4.
[18] O. K. Kovalev, in *Representation of the Crystallographic Space Group* (Eds.: H. T. Stokes, D. M. Hatch), Gordon and Breach Publishers, New York, **1993**.
[19] H. M. Rietveld, *J. Appl. Crystallogr.* **1969**, *2*, 65.
[20] J. Rodríguez-Carvajal, *Physica B* **1993**, *192*, 55.

Received June 23, 2004